Curves, Coriolis, and Cross-Channel Circulation in the Hudson River Estuary

MARGARET M. CONLEY[a] AND JAMES A. LERCZAK[a]

[a] *Oregon State University, Corvallis, Oregon*

(Manuscript received 30 May 2023, in final form 12 January 2024, accepted 19 January 2024)

ABSTRACT: Despite its relatively small magnitude, cross-channel circulation in estuaries can influence the along-channel momentum balance, dispersion, and transport. We investigate spatial and temporal variation in cross-channel circulation at two contrasting sites in the Hudson River estuary. The two sites differ in the relative strength and direction of Coriolis and curvature forcing. We contrast the patterns and magnitudes of flow at the two sites during varying conditions in stratification driven by tidal amplitude and river discharge. We found well-defined flows during flood tides at both sites, characterized by mainly two-layer structures when the water column was more homogeneous and structures with three or more layers when the water column was more stratified. Ebb tides had generally weaker and less definite flows, except at one site where curvature and Coriolis reinforced each other during spring tide ebbs. Cross-channel currents had similar patterns, but were oppositely directed at the two sites, demonstrating the importance of curvature even in channels with relatively gradual curves. Coriolis and curvature dominated the measured terms in the cross-channel momentum balance. Their combination was generally consistent with driving the observed patterns and directions of flow, but local acceleration and cross-channel advection made some notable contributions. A large residual in the momentum balance indicates that some combination of vertical stress divergence, baroclinic pressure gradients, and along-channel and vertical advection must play an essential role, but data limitations prevented an accurate estimation of these terms. Cross-channel advection affected the along-channel momentum balance at times, with implications for the exchange flow's strength.

SIGNIFICANCE STATEMENT: Currents that flow across the channel in an estuary move slower than those flowing along the channel, but they can transport materials and change water properties in important ways, affecting human uses of estuaries such as shipping, aquaculture, and recreation. We wanted to better understand cross-channel currents in the Hudson River estuary. We found that larger tides produced the strongest cross-channel currents with a two-layer pattern, compared to weaker currents with three layers during smaller tides. Higher or lower river flow also affected current strength. Comparing two locations, we saw cross-channel currents moving in opposite directions because of differences in the curvature of the river channel. Our results show how channel curvature and Earth's rotation combine to produce cross-channel currents.

KEYWORDS: Estuaries; Currents; Momentum; Secondary circulation; Subseasonal variability

1. Introduction

Circulation is central to the functioning of an estuary, impacting its biology and chemistry by advecting water properties such as temperature, salinity, dissolved oxygen, nutrients, and sediment. Circulation therefore affects many estuarine processes, from larval oyster settlement to eelgrass growth. An improved understanding of circulation is central to solving higher-order problems, including predicting how estuaries and the important ecosystem services they provide (Costanza et al. 1997) may respond to climate change and other human impacts.

But currents in estuaries are complicated. Transverse to the main along-channel flows are smaller cross-channel flows. Despite their small relative magnitude, these cross-channel currents can significantly affect the functioning of the entire estuarine system (e.g., Geyer and MacCready 2014). Flows across the channel can influence mixing (Seim and Gregg 1997), sediment transport (Fugate et al. 2007), and dispersion of tracers (Smith 1996). Cross-channel advection can also impact the along-channel momentum balance (Lerczak and Geyer 2004). Cross-channel currents are therefore critical for accurate estuarine modeling as well as our understanding of the broader estuarine environment.

Cross-channel currents are driven by multiple factors including Earth's rotation, channel curvature, and differential advection. Differential advection is important in well-mixed channels in which cross-channel shear in the along-channel flow generates cross-channel density gradients that can drive cross-channel flow cells (Nunes and Simpson 1985). Channel curvature drives cross-channel flows through local imbalances between the centrifugal force and the barotropic pressure gradient, which balances the centrifugal force in a depth-averaged sense (Chant 2010). This produces a two-layer flow pattern, which has been studied in rivers (e.g., Rozovskii 1957; Bathurst et al. 1977; Smith and McLean 1984) as well as relatively well-mixed channels in estuaries and near coastal headlands (e.g., Chant 2002; Geyer 1993). In stratified estuarine channels, it produces more complex patterns due to the

Denotes content that is immediately available upon publication as open access.

Corresponding author: Margaret M. Conley, conlemar@oregonstate.edu

DOI: 10.1175/JPO-D-23-0093.1

development of baroclinic pressure gradients (Chant and Wilson 1997; Lacy and Monismith 2001; Chant 2002; Nidzieko et al. 2009). Earth's rotation generates cross-channel circulation similarly to channel curvature, with the Coriolis force taking the place of the centrifugal force, producing a single rotating flow cell when vertical shear results in maximum along-channel flow at the surface (Chant 2010). Multiple vertical cross-channel flow layers can be generated when the boundary layer thickness is less than the estuary water depth and when a subsurface maximum occurs in the along-channel flow (Lerczak and Geyer 2004).

Stratification strongly influences cross-channel flows. Although a small amount of stratification can strengthen cross-channel flows by reducing mixing and enhancing vertical shear (Geyer 1993; Buijsman and Ridderinkhof 2008), strong stratification can suppress two-layer cross-channel flow (Lerczak and Geyer 2004). Two-layer cross-channel flows tilt isopycnals laterally and generate baroclinic pressure gradients that oppose the original forcing, producing more complex, multilayer patterns in contrast to simpler two-layer flows during well-mixed conditions (Chant 2002; Nidzieko et al. 2009). Variability in stratification can cause changes in cross-channel flow on multiple time scales. Partially mixed estuaries like the Hudson River can range from relatively well-mixed during spring tides or low-discharge conditions to strongly stratified during neap tides or high discharge (Geyer and Chant 2006). Within the tidal cycle, tidal straining causes some estuaries to be more stratified during ebb than flood (Simpson et al. 1990), leading to weaker ebb tide cross-channel flows, as found for a modeled straight channel (Lerczak and Geyer 2004).

Although our understanding of cross-channel flows has expanded in recent years, few studies have examined the combination of Coriolis and curvature forcing in an estuarine channel where the forcings are of similar magnitude (Fugate et al. 2007; Buijsman and Ridderinkhof 2008). The relative importance of Coriolis and curvature forcing depends on the radius of curvature as well as the magnitude and vertical shear of the along-channel tidal velocity and the estuary's latitude. Several studies have focused on the combination of curvature forcing and baroclinic pressure gradients in sharply curved channels where Coriolis forcing is unimportant (Lacy and Monismith 2001; Chant 2002; Nidzieko et al. 2009; Kranenburg et al. 2019), or, conversely, Coriolis forcing in mostly straight channels where curvature is unimportant (Valle-Levinson et al. 2000; Ott et al. 2002). But understanding how curvature combines with Coriolis is important to developing a complete understanding of cross-channel flows and their impacts on broader estuarine dynamics. Studies have examined the interplay of these two forces in oceanic flows around islands and in submarine channels (Alaee et al. 2004; Cossu and Wells 2010). Coriolis and curvature forcing share a similar structure in the cross-channel momentum balance. However, Coriolis forcing changes sign depending on the direction of the along-channel tidal flow, whereas the sign of curvature forcing is independent of the along-channel flow direction. This can contribute to tidal asymmetry in the strength and structure of cross-channel flows, depending on whether the two forcings reinforce or counteract each other (Fugate et al. 2007; Buijsman and Ridderinkhof 2008).

In this study, we investigate cross-channel currents in the Hudson River estuary to understand the combination of Coriolis and curvature forcing. The broad range of stratification in the Hudson provides an ideal environment to explore these dynamics. We first investigate how along- and cross-channel currents vary over space and time in the Hudson (section 3b). To understand spatial variability, we compare the patterns and magnitudes of flows over a semidiurnal tidal cycle at two sites that differ in both the magnitude and sign of their radii of curvature. To understand temporal changes, we analyze variation in currents for a range of forcing conditions, including spring and neap tides during high and low discharge. We next compare terms in the cross-channel momentum balance between the two sites and during different forcing conditions to identify important factors controlling the cross-channel flow, in particular the relative magnitude of Coriolis and curvature forcing and the relative importance of other terms [section 3c(1)]. We finally explore the impact of cross-channel advection on the along-channel momentum balance to better quantify the influence of cross-channel flows on broader estuarine dynamics [section 3c(2)].

2. Methods

a. Momentum balance

1) Cross-channel momentum balance

A natural orthogonal curvilinear coordinate system with which to examine the momentum balance in a meandering estuary is one which distinguishes streamwise (along-channel v) from streamnormal (cross-channel u) flows (Kalkwijk and Booij 1986; Nidzieko et al. 2009; Smith and McLean 1984). This is well approximated by a local polar coordinate frame, giving the following cross-channel momentum budget:

$$\frac{\partial u}{\partial t} = -\mathbf{u}\cdot\nabla u + fv + \frac{v^2}{R} - g\frac{\partial \eta}{\partial x} - \frac{g}{\rho_0}\int_z^\eta \frac{\partial \rho}{\partial x}dz' + \frac{\partial}{\partial z}K(z,t)\frac{\partial u}{\partial z}, \tag{1}$$

in which $\mathbf{u}$ is the velocity vector (u, v, w), f is the Coriolis parameter, R is the local channel radius of curvature (positive curving to the left, looking upriver), g is gravitational acceleration, η is the sea surface height, ρ is water density, ρ_0 is a reference density, and K is the time- and depth-dependent eddy viscosity. The terms, from left to right, are local acceleration, advection of gradients in the cross-channel velocity, Coriolis forcing, curvature forcing, barotropic and baroclinic pressure gradients, and vertical stress divergence. For the right-handed coordinate system used here, positive v is directed up-estuary. This momentum balance demonstrates the influence of both curvature and Coriolis on cross-channel flows. The sign of Coriolis forcing is dependent on the direction of the along-channel tidal flow, whereas the sign of curvature forcing is independent of along-channel tidal flow direction (because the forcing is quadratic in v).

The barotropic pressure term can be removed by subtracting the depth-averaged momentum balance from Eq. (1):

$$\frac{\partial u}{\partial t} = -(\mathbf{u}\cdot\nabla u - \overline{\mathbf{u}\cdot\nabla u}) + f(v-\overline{v}) + \frac{v^2-\overline{v^2}}{R} - \frac{g}{\rho_0}\left(\int_z^\eta \frac{\partial \rho}{\partial x}dz' - \overline{\int_z^\eta \frac{\partial \rho}{\partial x}dz'}\right) + \frac{\partial}{\partial z}K(z,t)\frac{\partial u}{\partial z} + \frac{1}{H}K(z,t)\frac{\partial u}{\partial z}\bigg|_{z=-H}. \quad (2)$$

The overbar indicates depth averaging, and $z = -H$ is at the estuary bottom, with z increasing upward and $z = 0$ at the mean water surface. We assume that $\overline{u}$ and the surface stress are negligible.

A natural nondimensional parameter to assess the relative importance of curvature and Coriolis forcing in the cross-channel momentum balance is the ratio of the depth and tidal average of the absolute value of those two terms in Eq. (2), which we define as γ:

$$\gamma = \frac{1}{fR}\frac{\left\langle\left|\overline{v^2}-\overline{v^2}\right|\right\rangle}{\left\langle\left|v-\overline{v}\right|\right\rangle}, \quad (3)$$

where the angle brackets indicate averaging over the semidiurnal period. When $|\gamma| > 1$, curvature forcing dominates over Coriolis forcing. The sign of γ indicates the direction of the curve along the channel as well as the tidal phase when curvature and Coriolis forcing act together to drive cross-channel flows. For example, when $\gamma > 0$, curvature and Coriolis have the same sign during flood tide and produce stronger combined forcing during flood than ebb, when they act against each other. The parameter γ is similar to the Rossby number described by Geyer (1993) that compares the maximum cross-channel flows driven by curvature and Coriolis for a logarithmic along-channel flow profile.

A second nondimensional parameter, which we define as β, indicates the significance of the cross-channel flow in estuarine transport and dynamics, giving a scale for the fraction of the channel width over which cross-channel currents can transport a given tracer over a characteristic time scale:

$$\beta = \frac{T}{B}\left\langle\left|\overline{u^2}-\overline{u^2}\right|\right\rangle^{1/2}, \quad (4)$$

where T is a time scale reflecting the persistence of consistent lateral flows and B is the channel width. Thus, when $\beta \sim 1$, we expect water parcels to be advected a substantial fraction of the channel width by the cross-channel flow and the cross-channel flow to have a significant impact on momentum budgets and tracer dispersion.

Both γ and β vary by site because of differences in width and curvature radius as well as over time as the cross-channel flows vary in strength with changes in tidal amplitude and river discharge.

2) ALONG-CHANNEL MOMENTUM BALANCE

Following the same conventions used for the cross-channel momentum balance, the along-channel momentum balance is given by

$$\frac{\partial v}{\partial t} = -\mathbf{u}\cdot\nabla v - g\frac{\partial \eta}{\partial y} - \frac{g}{\rho_0}\int_z^\eta \frac{\partial \rho}{\partial y}dz' + \frac{\partial}{\partial z}K(z,t)\frac{\partial v}{\partial z}. \quad (5)$$

The contributions of curvature and Coriolis to the along-channel balance are negligible due to the small relative magnitude of the cross-channel flow. The barotropic pressure term can again be removed by subtracting the depth-averaged momentum balance from Eq. (5):

$$\frac{\partial(v-\overline{v})}{\partial t} = -(\mathbf{u}\cdot\nabla v - \overline{\mathbf{u}\cdot\nabla v}) - \frac{g}{\rho_0}\left(\int_z^\eta \frac{\partial \rho}{\partial y}dz' - \overline{\int_z^\eta \frac{\partial \rho}{\partial y}dz'}\right) + \frac{\partial}{\partial z}K(z,t)\frac{\partial v}{\partial z} + \frac{1}{H}K(z,t)\frac{\partial v}{\partial z}\bigg|_{z=-H}. \quad (6)$$

We again assume that the surface stress is negligible.

A comparison of the relative sizes of the along-channel acceleration and the cross-channel advection of gradients in along-channel flows indicates the relative importance of the cross-channel flow to the along-channel dynamics.

b. Data collection and processing

1) STUDY SITES

We compare along- and cross-channel currents at two sites within the Hudson River estuary: Lincoln Harbor (LH) and Spuyten Duyvil (SD) (Fig. 1). The channel at SD has a radius of curvature of approximately 17 km. At LH, the radius is approximately −5 km. These radii were estimated using the channel centerline, calculated as the average position of the 10-m isobaths on each side of the channel, following the method of Smith and McLean (1984). We further verified these values by drawing arcs of the calculated radii on a map of the channel to compare visually with the channel curves (see Fig. 1). To compare the average characteristics of the two sites, we can estimate γ using a characteristic along-channel current speed scale V:

$$\gamma_{\text{est}} = \frac{V}{fR}. \quad (7)$$

Using $V = 1$ m s^{-1} produces an estimated γ of −2.1 at LH, compared to 0.6 at SD. We therefore expect Coriolis to be slightly more important than curvature at SD, with the reverse being true at LH. Looking upstream, the channel curves to the right at LH and to the left at SD, producing curvature forcing in opposite directions. Since $\gamma < 0$ at LH, curvature and Coriolis forcing are additive during ebb tide, whereas they are additive during flood tide at SD where $\gamma > 0$. More details on how γ varies with forcing at the two sites are provided in the discussion (section 4b).

The two sites have similar thalweg depth and along-channel flow magnitude and vertical structure; however, their bathymetry differs due to dredging at the downstream site, with a more symmetric structure at LH compared to a shallow western shoal and deeper eastern channel at SD (Fig. 2). Based on our analyses, $T \approx 3$ h and $B = 0.95$ and 1.63 km at LH and SD, respectively.

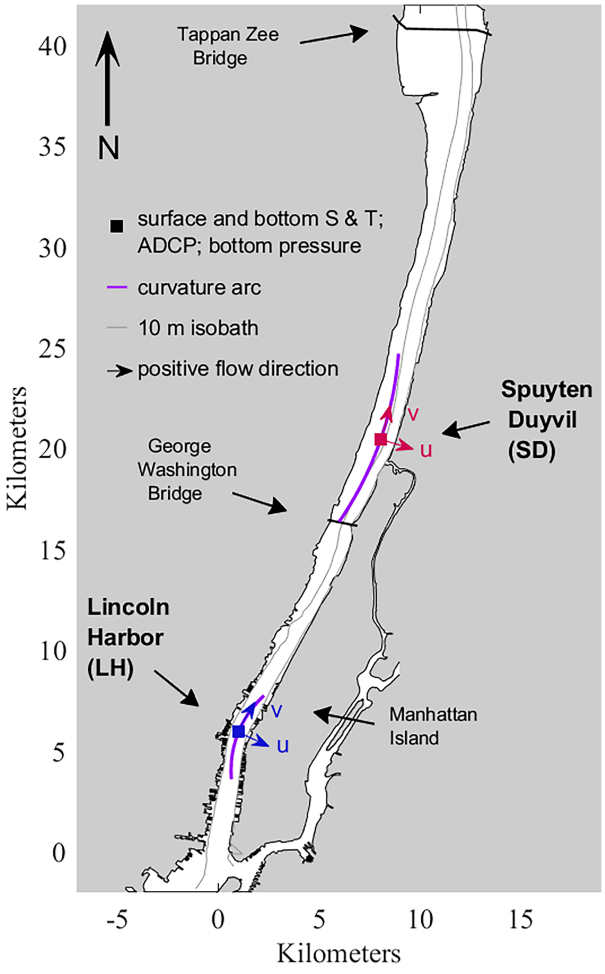

FIG. 1. Map showing the lower Hudson River and the locations of the two study sites, Lincoln Harbor (LH) and Spuyten Duyvil (SD). The S denotes salinity (a conductivity sensor) and T denotes temperature. In 2002, a cross-channel array was deployed at SD, with four ADCPs and multiple S and T measurements. In 2004, a single ADCP was deployed in the thalweg at both SD and LH, with one S and T measurement at the surface and one at the bottom. Purple arcs show the radius of curvature at each site; $R = -5$ km at LH and $R = 17$ km at SD, with a positive radius indicating that the channel curves to the left looking upstream. The gray lines show the 10-m isobaths. Arrows indicate the directions of positive along-channel (v) and cross-channel (u) flow at each site.

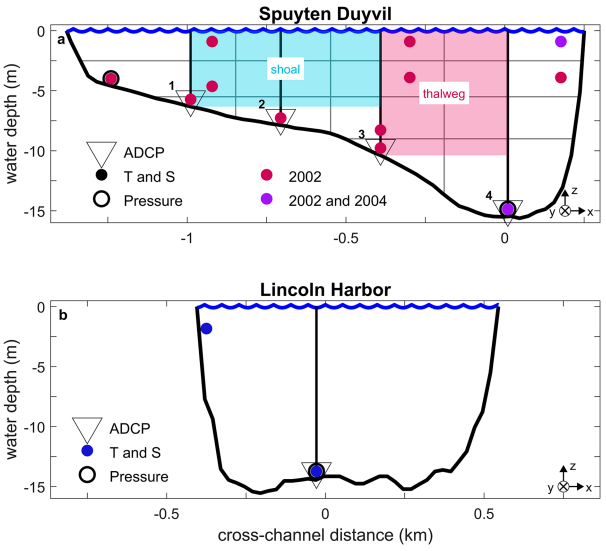

FIG. 2. Cross sections of the channel at (a) Spuyten Duyvil and (b) Lincoln Harbor showing bathymetry and instrument locations. In (a), gray lines show the borders of 14 regions for which Lerczak et al. (2006) calculated salinity and temperature values using objective mapping, which we used to calculate cross-channel density gradients for the 2002 data. Vertical black lines show the locations of ADCP current measurements. The turquoise and red boxes show the areas represented by the shoal and thalweg momentum balances for the 2002 data.

2) DATASETS

This study uses data collected in two separate field experiments conducted in the spring of 2002 (Geyer et al. 2023; Lerczak et al. 2006; Chant et al. 2007) and the spring and summer of 2004 (Lerczak et al. 2023; Ralston et al. 2008; Lerczak et al. 2009). The 2004 study included both sites. Upward-looking ADCPs and bottom conductivity, temperature, and pressure sensors were deployed in the thalweg at each site, attached to tripods. The ADCP transducer heads and the sensors were 0.7 m above the bottom. Surface temperature and conductivity sensors were attached to surface moorings or pier pilings approximately 1 m below the surface. Temperature, conductivity, and pressure measurements were recorded every 5 min, whereas average currents were recorded every 15 min at LH and every 5 min at SD, using a vertical bin width of 0.25 m. The data record covers 108 days, from 24 March to 11 July 2004. Although this dataset captures the greatest variability in tidal amplitude and discharge conditions, it has no cross-channel resolution and limited vertical resolution of water properties.

The 2002 dataset includes detailed measurements of the water column at only one site, SD. A cross-channel array of salinity and temperature sensors, along with four ADCPs and two pressure sensors flanking the channel, allow for the calculation of both cross-channel density gradients and cross-channel advection. The ADCP transducer heads were 0.6 m above the bottom and the ADCPs used a vertical bin width of 0.25 m. Data were collected for a period of 43 days, from 23 April to 5 June 2002. Current velocities were recorded every 15 min, and temperature, conductivity, and pressure every 5 min.

3) DATA PROCESSING

Currents were extrapolated to the bottom and to the tidally varying sea surface following the methods of Lerczak et al. (2006). The surface was identified by locating the peak in the ADCP backscatter signal, and data from the upper 10% of the water column were removed to minimize side-lobe contamination. We then fitted a parabola to the uppermost six remaining data points, requiring zero shear at the surface. Although this process occasionally enhanced cross-channel

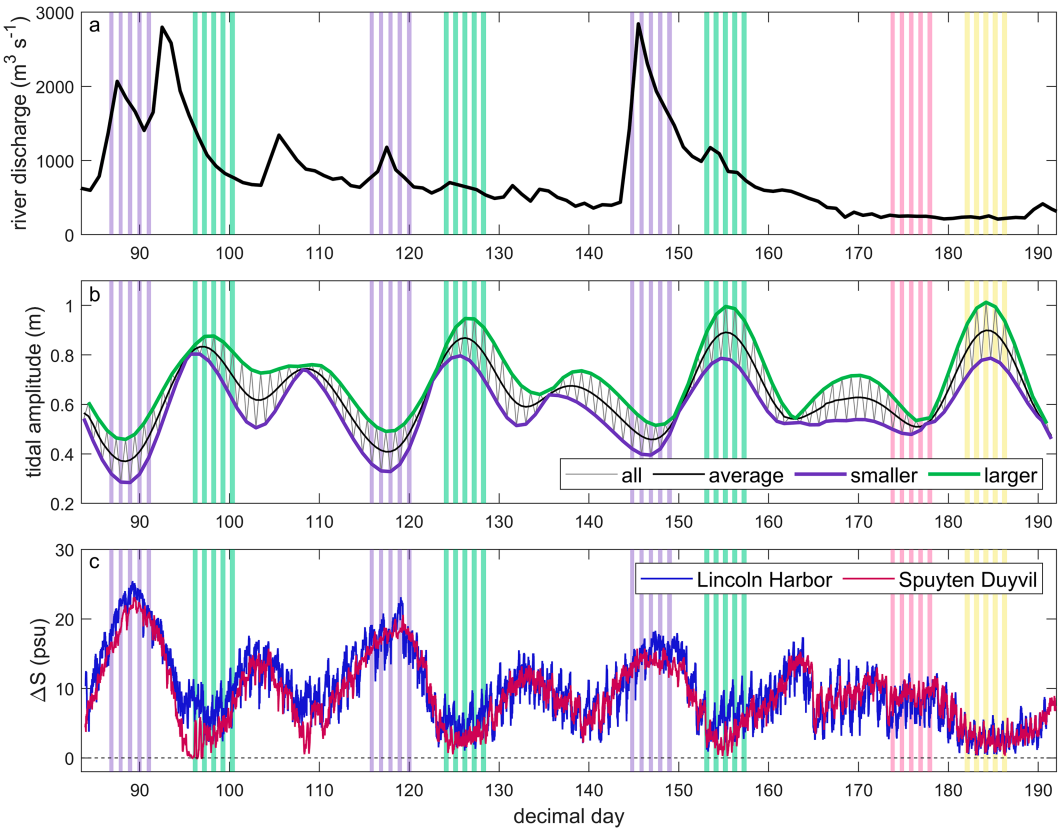

FIG. 3. Time series of (a) river discharge, (b) tidal amplitude, and (c) stratification for the 2004 study period. Shading denotes the time periods corresponding to the four regimes of flow compared in this study: neap tides and spring tides during high and low discharge. For high (low) discharge, neap conditions are shaded in purple (red) and spring conditions are shaded in green (yellow). In (b), the gray line shows the amplitude of each semidiurnal tidal cycle. The thick purple and green lines show the smaller- and larger-amplitude tidal cycles, respectively. The black line shows the average tidal amplitude. In (c), stratification is shown for both LH (blue) and SD (red).

flow velocities at the surface, the calculated velocities matched the observed near-surface currents better than simply extending the average near-surface flow to the surface. Currents were extrapolated to the bottom by fitting near-bottom currents to a log-layer profile, given by

$$u(z + H) = \frac{u^*}{\kappa} \ln\left(\frac{z + H}{z_0}\right), \tag{8}$$

with z_0 set to 0.067 m and where κ is the von Kármán constant and H is the depth at each site (Lerczak et al. 2006). We calculated u^* using the bottommost data point. Fitting the currents to a parabola, imposing a zero value at the bottom, produced similar results. Current velocity data were rotated into along- and cross-channel components using an EOF analysis of the depth-averaged transport vector $(\overline{u}H, \overline{v}H)$ to align the along-channel direction with the principal axis of the transport vector.

River discharge was obtained from the USGS gauge at the Green Island Dam (U.S. Geological Survey 2016) and scaled by a factor of 1.6 to account for the portion of the watershed between the study sites and the gauge (Lerczak et al. 2006).

c. *Forcing regimes*

We used pressure, salinity, and river discharge data to identify different forcing regimes based on tidal amplitude and river discharge conditions. Defining low discharge as flow consistently less than 300 m^3 s^{-1}, we distinguished periods of high and low flow (Figs. 3a and 4a). Pressure records were used as a proxy for tidal amplitude. We used a harmonic analysis of the pressure record (Pawlowicz et al. 2002) to identify spring and neap tides as periods of high and low semidiurnal tidal amplitude, respectively. We calculated a time series of tidal amplitude as the difference in height between each high and subsequent low tide, divided by two. Since individual semidiurnal tidal cycles tend to alternate between smaller and larger amplitudes, we then applied a low-pass filter over four semidiurnal tidal cycles to derive an average tidal amplitude time series. We focused on spring tides with larger tidal amplitudes and neap tides with smaller tidal amplitudes (Figs. 3b and 4b), because these conditions exhibited the greatest contrast in flow characteristics. The 2004 study period included three periods of larger spring tides and smaller neap tides that coincided with high discharge and one that coincided with low discharge. We used the

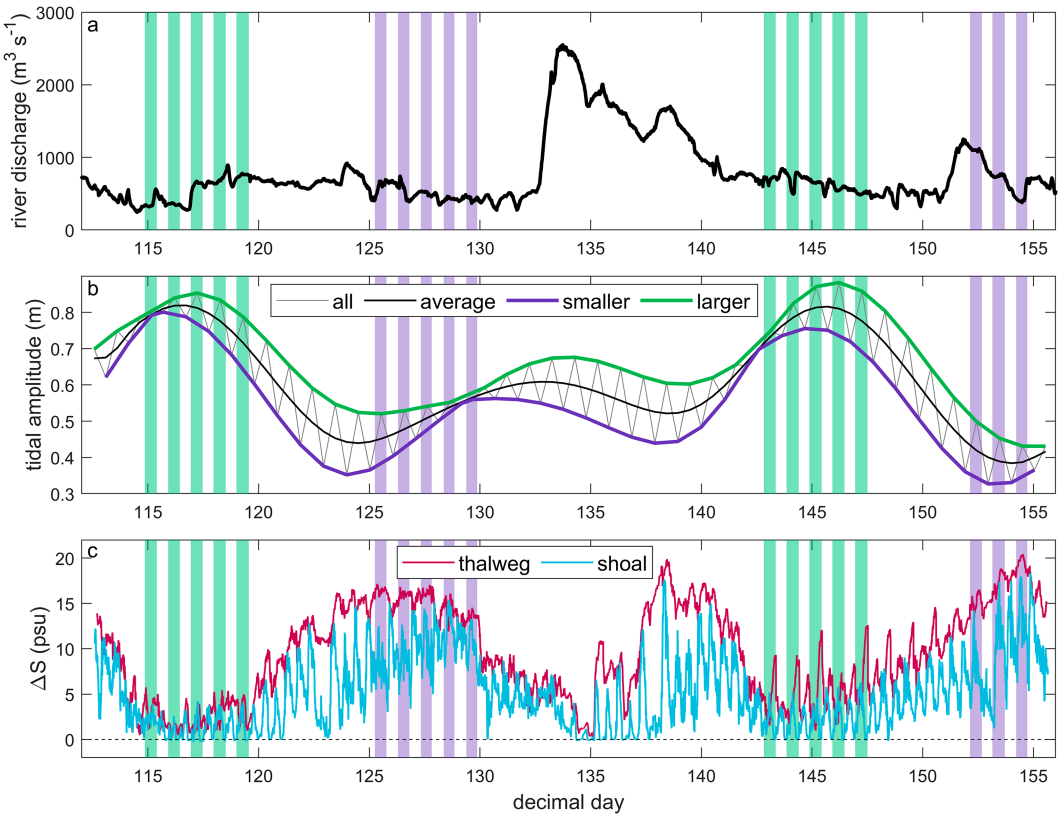

FIG. 4. Time series of (a) river discharge, (b) tidal amplitude, and (c) stratification for the 2002 study period. Shading denotes the time periods corresponding to two regimes of flow: neap tides (purple) and spring tides (green) during high discharge. In (b), the gray line shows the amplitude of each tidal cycle. The thick purple and green lines show the smaller- and larger-amplitude tidal cycles, respectively. The black line shows the average tidal amplitude. In (c), stratification is shown for both shoal (turquoise) and thalweg (red) locations, near sites 1 and 4, respectively (see Fig. 2).

difference between bottom and surface salinity as an indicator of stratification (Figs. 3c and 4c).

Based on these criteria, for the 2004 data, we identified four regimes of flow that were well characterized by our dataset, including spring tides and neap tides during high discharge and low discharge (Fig. 3). Discharge was high for most of the 2002 study period, so we differentiated only between spring and neap tides (Fig. 4).

d. Semidiurnal phase averaging

Along- and cross-channel currents, water level, stratification, density, and momentum balance terms were semidiurnal phase averaged to obtain characteristic values over a semidiurnal tidal cycle for the four forcing regimes described above. The phase-averaging process involved two steps. First, tidal cycles for each variable were interpolated onto a common semidiurnal time base, with $t = 0$ being the transition from ebb to flood, as determined by the time when the depth-averaged along-channel flow (with the low-frequency component removed using a low-pass filter with a half-amplitude period of 33 h) was zero, and $t = 1$ being the end of the semidiurnal tidal cycle (the subsequent transition from ebb to flood). Second, interpolated tidal cycles sharing the same forcing regime were averaged together to give a representative tidal time series for each variable and regime.

We identified time periods that met the criteria of the four regimes and chose five tidal cycles during each time period that showed the most consistent currents and stratification and the lowest (for neap regimes) or highest (for spring regimes) tidal amplitude to average together. Every other tidal cycle was included in the average because the cycles tend to alternate in magnitude. In general, the larger-amplitude cycles were included in spring tide averages and the smaller cycles in neap tide averages to emphasize the contrast in tidal amplitude. Neap tidal cycles in 2002 (see purple shading in Figs. 4b,c) were exceptional in two ways. First, during the period from days 125 to 130, larger-amplitude tidal cycles occurring a few days after the minimum in tidal amplitude were used in the semidiurnal phase averaging because they demonstrated more consistently high stratification both on the shoal and in the thalweg. Second, the end of the time series limited the number of available suitable cycles to three for the second period included in the neap forcing regime. To evaluate whether the averages accurately represent the general flow patterns during these conditions, we both visually compared individual tidal cycles with the resulting averages and calculated the standard

deviation of the cross-channel currents at each depth and time point across all the tidal cycles included in each average. The standard deviations of the cross-channel currents for each regime averaged less than 0.04 m s^{-1} over the tidal cycle, compared to peak cross-channel current magnitudes of 0.20 m s^{-1} or more.

e. *Momentum balance analyses*

1) CROSS-CHANNEL MOMENTUM BALANCE ANALYSIS

With the data available, we calculated as many terms as possible in the cross-channel momentum balance [Eq. (2)] to determine the dominant forcing terms at the two sites during different regimes. Using the 2004 dataset, we calculated the local acceleration, Coriolis, and curvature terms. For the 2002 dataset at SD, we additionally calculated cross-channel (x-c) advection and cross-channel density gradients, which we used to infer potential baroclinic forcing. The residual includes vertical stress divergence, the unknown advective terms, the baroclinic pressure gradient, measurement noise, and calculation errors from approximating gradients and integrals, as well as cross-channel advection for the 2004 data:

$$\underbrace{\frac{\partial u}{\partial t}}_{\text{local acceleration}} = \underbrace{-\left(u\frac{\partial u}{\partial x} - u\overline{\frac{\partial u}{\partial x}}\right)}_{\text{x-c advection}} + \underbrace{f(v-\overline{v})}_{\text{Coriolis}} + \underbrace{\frac{v^2-\overline{v^2}}{R}}_{\text{curvature}} + \text{residual}. \quad (9)$$

We low-passed the cross-channel currents (u) and the density (ρ) using a cutoff period of 2 h to focus our analysis on the time scales of interest to this study. This removed high-frequency noise from the local acceleration term in particular, as well as the advection term. The along-channel flow (v) was not filtered since its high-frequency variability was not as apparent.

The terms in the momentum balance for the 2002 dataset were calculated for two separate horizontal regions based on available current data: between the first and third ADCPs, representing the shoal, and between the third and fourth ADCPs, representing the thalweg. Current speeds u and v were derived from ADCP 2 for the shoal and the average of ADCPs 3 and 4 for the thalweg (see Fig. 2). Cross-channel gradients were calculated as the average of the gradients between ADCPs 1 and 2 and ADCPs 2 and 3 for the shoal, and as the gradient between ADCPs 3 and 4 for the thalweg. Terms were only calculated for depths where data were available on both sides of each region. The depth-averaged terms are therefore approximated as the depth average over the vertical range for which there is data, limited by the shallower side of each region.

Cross-channel density gradients were derived from the salinity and temperature of the 14 regions indicated with gray lines in Fig. 2, which Lerczak et al. (2006) calculated using objective mapping. The density was calculated from temperature, salinity and pressure using the GSW Oceanographic Toolbox (McDougall and Barker 2011) and low-passed with a cutoff period of 2 h. Vertical density profiles were constructed for each of the four horizontal regions (approximately centered about each ADCP), and gradients were calculated between adjacent regions, using the average midpoint of each region as the horizontal position. The density gradients calculated between the regions containing ADCPs 1 and 2 and ADCPs 2 and 3 were averaged to obtain values for the shoal, and the gradient between the regions containing ADCPs 3 and 4 was used to represent the thalweg. A vertical linear interpolation between T and S sensors above and near each ADCP produced similar results during spring tides, but not during neap tides. Cross-sectional transects collected by boat during the 2002 experiment (Lerczak et al. 2006) indicate a sharp pycnocline during neap tides that is difficult to capture with the available sensor resolution. The objective mapping estimates provide an improvement over a linear vertical interpolation in these cases, but the estimated values still have large uncertainty due to poor resolution of the pycnocline. The density gradients enable a qualitative assessment of the potential baroclinic forcing.

The cross-channel density gradients and the momentum balance terms were phase averaged using the same process as for the currents, allowing us to compare between the two sites and among the different regimes.

2) ALONG-CHANNEL MOMENTUM BALANCE ANALYSIS

Using the 2002 dataset, we calculated two terms in the along-channel momentum balance with the depth average removed [Eq. (6)]: local acceleration and cross-channel advection (the cross-channel advection of cross-channel gradients in the along-channel flow). Current speeds and horizontal gradients were calculated as described in the previous section for the same two horizontal regions, shoal and thalweg.

3. Results

a. *Trends in stratification and its dependence on discharge and tidal amplitude*

Stratification was enhanced by both small tidal amplitude and high river discharge. Stratification peaked during neap tides and decreased to near-zero values during spring tides (Figs. 3c and 4c). Smaller-amplitude spring tides and neap tides also had greater average stratification than larger-amplitude spring and neap tides, respectively, especially in 2004. Although the influences of river discharge and tidal amplitude are confounded, high-discharge events during the first neap tide in 2004 (centered on day 89; Fig. 3) and during a larger-amplitude neap tide in 2002 (centered on day 138; Fig. 4) enhanced stratification, and the low-discharge period at the end of the 2004 study coincided with lower stratification. Spuyten Duyvil (SD), which is farther upriver, tended to have slightly lower stratification on average for the same time periods and conditions compared to Lincoln Harbor (LH), except during low-discharge neap tides (Fig. 5).

Stratification within the tidal cycle varied in a complex manner by as much as 8 psu, and with strong dependence on forcing. In 2004, spring tides and low-discharge neap tides at LH tended to have stronger stratification during the first half of flood and minimum stratification during the second half of flood or during ebb (Figs. 5e–g). The same was true of SD for

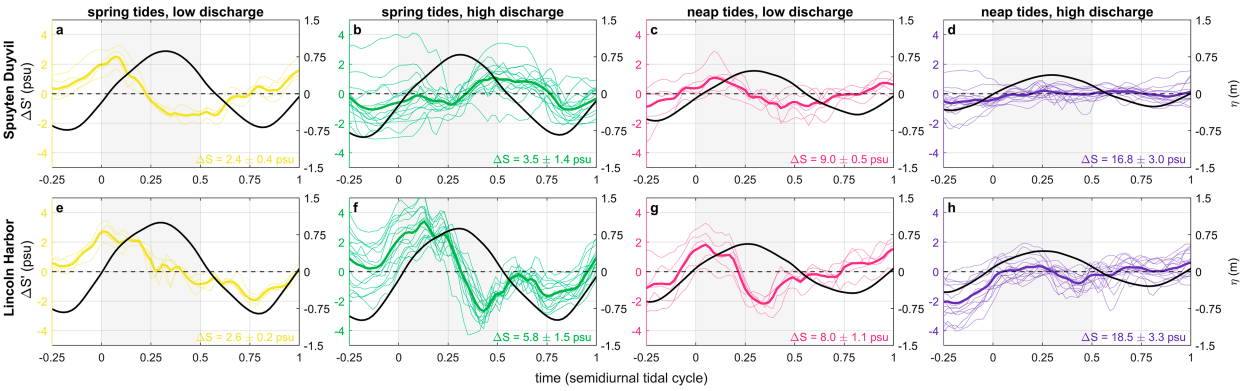

FIG. 5. Tidal variation in stratification, relative to the mean value for each tidal cycle, at (top) SD and (bottom) LH for the 2004 study period (left *y* axis). Stratification is defined as bottom minus surface salinity. Shown are each tidal cycle (thin lines) and the overall average (thick line) for each regime, with colors corresponding to the regimes shown in Fig. 3. Time starts just before the transition from ebb to flood and ends at the end of ebb; flood times are highlighted in gray shading. The thick black line shows the average water level variations for each regime (right *y* axis). The average stratification over the tidal cycle ± one standard deviation is listed in the bottom-right corner of each panel.

low-discharge spring and neap tides (Figs. 5a,c), but not for spring tides with high discharge, which had higher stratification during late flood and early ebb tide (Fig. 5b). Stratification was consistently high during neap tides with high discharge (Figs. 5d,h). Because individual semidiurnal tidal cycles alternated between smaller and larger amplitudes, stratification did not necessarily show a return to preflood values at the end of each ebb.

Tidal variations in stratification also differed across the channel at SD in 2002 (Fig. 6). On the shoal, stratification tended to peak around maximum flood (during neap tides) or early ebb (during spring tides), with a shift to slightly later times moving from the shoal to the thalweg. The patterns at the deepest site (site 4) were similar to the 2004 high-discharge data, except that in 2002 spring tide stratification peaked later in ebb.

b. *Patterns of along- and cross-channel circulation*

1) ALONG-CHANNEL CURRENTS

Along-channel flow patterns and magnitudes varied with tidal amplitude and river discharge. Peak ebb currents were always fastest at the surface, whereas peak flood currents had a subsurface maximum at depths of 5–10 m during neap tides (Figs. 7 and 8). Peak flood currents during spring tides were fastest at the surface in all cases except for high discharge at LH, where flow peaked about 5 m below the surface (Fig. 7f). In general, the transition from flood to ebb tide in the along-channel currents occurred synchronously over depth, except during neap tides with high discharge, for which the transition at both the surface and bottom occurred earlier than at middepth by about 2.5 and 1 h, respectively. The transition from ebb to flood occurred first at the bottom and last at the surface, with the longest

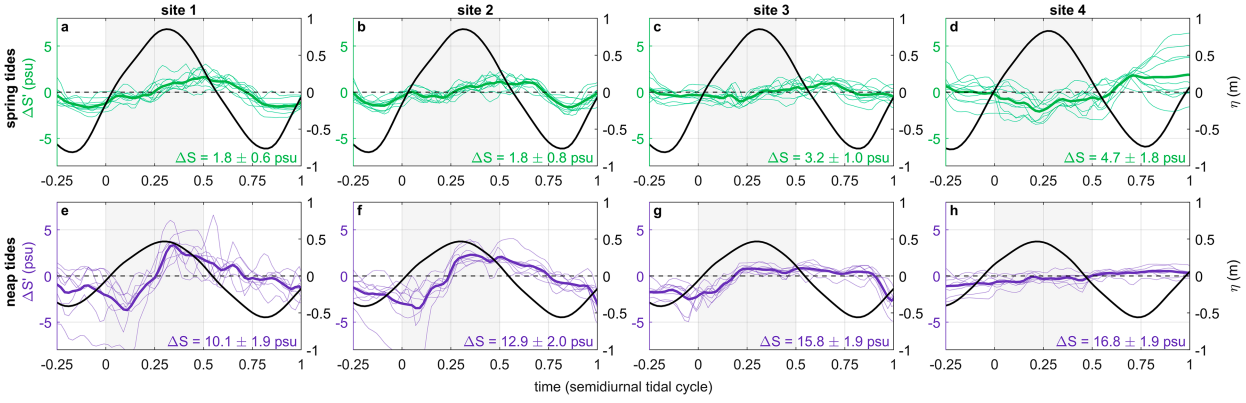

FIG. 6. Tidal variation in stratification (bottom minus surface salinity), relative to the mean value for each tidal cycle, for (top) spring tides and (bottom) neap tides at SD for the 2002 study period (left *y* axis). The four sites span the channel from west to east. Shown are each tidal cycle (thin lines) and the overall average (thick line) for each regime, with colors corresponding to the regimes shown in Fig. 4. Time starts just before the transition from ebb to flood and ends at the end of ebb; flood times are highlighted in gray shading. The thick black line shows the average water level variations (right *y* axis). The average stratification over the tidal cycle ± one standard deviation is listed in the bottom right corner of each panel.

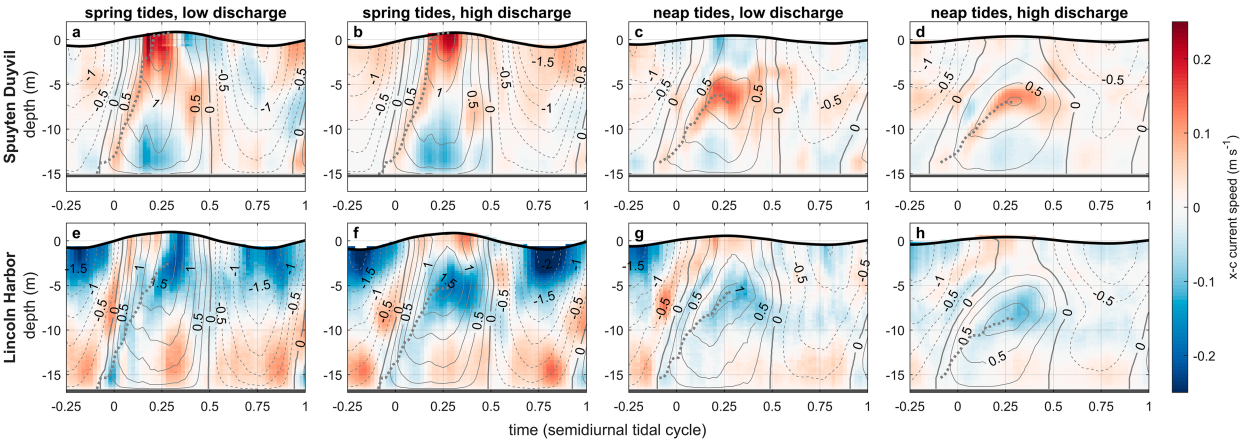

FIG. 7. Semidiurnal phase-averaged currents during four regimes at (top) SD and (bottom) LH for the 2004 study period. The time periods included in these averages are highlighted in yellow, green, red, and purple, respectively, in Fig. 3. Time starts just before the beginning of flood and ends at the end of ebb. Depth ranges from zero at the mean water surface to the thalweg depth at each site. Along-channel currents are shown as contours; dashed lines indicate negative (oceanward) velocities. Cross-channel (x-c) currents are shown as colors, with red indicating positive (eastward) velocities and blue indicating negative (westward) velocities. The dotted gray lines track the upward movement of the maximum in along-channel flow during the first half of flood tide.

difference (about 4 h) occurring during neap tides with high discharge. A subsurface maximum in along-channel flooding flow moved upward from the bottom, reaching the surface after about 3.5 to 4.5 h during most spring tides (except LH, high discharge). During neap tides, the maximum tended to move upward more slowly (about 4.5–5 h) and did not reach the surface.

2) CROSS-CHANNEL CURRENTS

Cross-channel currents also exhibited variability both within and among tidal cycles. During peak flood of neap tides, the cross-channel flow had a three-layer pattern. In contrast, during peak flood of spring tides, the cross-channel flow generally had a two-layer pattern, with the exception of the three-layer flow during high discharge at LH (Fig. 7f). During neap ebb tides, cross-channel flows were generally weak. In contrast, spring ebb tides were characterized by strong two-layer flows at LH, and weaker, less distinct flows at SD, sometimes with a two-layer structure during the later part of ebb just before along-channel currents began to flood at the bottom (e.g., Fig. 7a, times 0.75–0.9). This pattern was more apparent and developed earlier in ebb in 2002 (Fig. 8d) than in 2004.

Cross-channel flows during the transition periods from ebb to flood and from flood to ebb exhibited multiple (as many as four) layers during all regimes. This was particularly apparent during the ebb to flood transition, when cross-channel flows were initially close to zero at the bottom. Soon after the ebb to flood transition in the along-channel flow, a cross-channel flow developed at the bottom (eastward at SD and westward at LH) as a thin layer that propagated up the water column, tracking the subsurface maximum in the along-channel flooding currents, and with layers of opposing cross-channel flow above and below. If the maximum in along-channel velocity

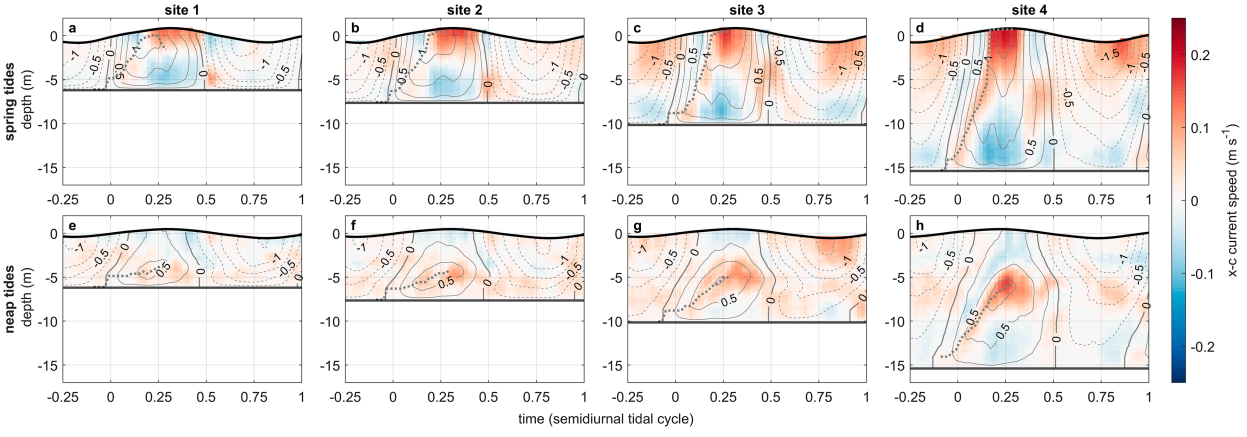

FIG. 8. Semidiurnal phase-averaged currents during (top) spring tides and (bottom) neap tides with high discharge at SD for the 2002 study period. The locations of sites 1–4 (see Fig. 2a) cross the channel from west to east. The time periods included in these averages are highlighted in purple (neap) and green (spring) in Fig. 4. Axes, contouring, and shading are the same as in Fig. 7.

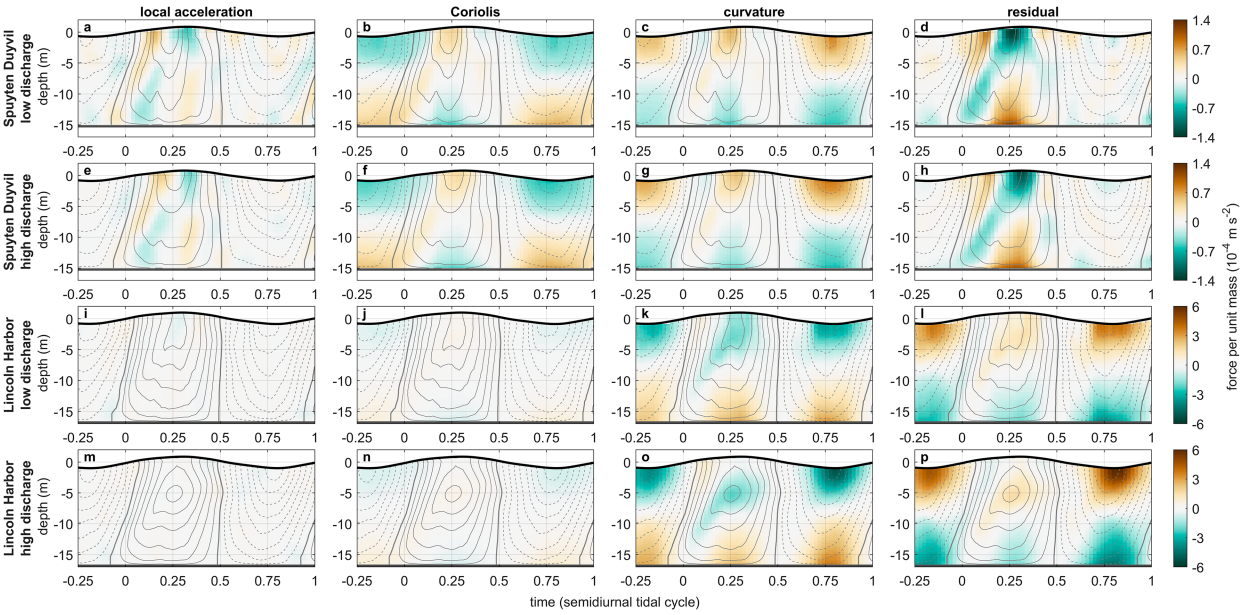

FIG. 9. Semidiurnal phase-averaged cross-channel momentum balance terms (with the depth average removed) during low- and high-discharge spring tides at (a)–(h) SD and (i)–(p) LH for the 2004 study period. Time runs from just before the beginning of flood to the end of ebb. Depth ranges from zero at the mean water surface to the thalweg depth at each site. The magnitude of each term is shown in color, with brown (green) indicating eastward (westward) forcing. Note that scales differ between the two sites. The last panel in each row shows the sum of the first panel minus the middle two panels. Contours show the average along-channel flow (solid lines for flooding flow and dashed lines for ebbing flow at 0.25 m s^{-1} intervals, with a thicker solid line at zero flow).

reached the surface, a two-layer cross-channel flow resulted at peak flood. If a subsurface maximum persisted throughout the flood phase, a three-layer cross-channel flow resulted.

At SD in 2002, cross-channel flows on the shoal shared some features with the thalweg currents (Fig. 8). Two-layer flows during neap flood tides corresponded with the upper two of the three layers of thalweg flow. During spring flood tides, the shoal retained the same two-layer pattern as the thalweg, but with both layers compressed to fit within the smaller water depth. As in 2004, cross-channel currents were usually stronger and better defined during flood than ebb.

While many of the qualitative patterns in the cross-channel flow at SD and LH were similar, particularly during flood tide, the directions of the respective cross-channel flow layers were opposite, reflecting a difference in the relative importance of Coriolis and curvature forcing as well as the sign of curvature forcing. The two sites also differed in spring tide flood–ebb changes in current strength; whereas currents were stronger and maintained a clear pattern during ebb at LH (Figs. 7e,f), they were stronger during flood at SD (Figs. 7a,b), where the pattern during ebb was less distinct. The three-layer flow at LH during high-discharge spring tides was also unique.

c. *Momentum balance analysis*

1) CROSS-CHANNEL MOMENTUM BALANCE

Measured terms in the cross-channel momentum balance (with the depth average removed from each term) differed both among forcing regimes and between the two sites (Figs. 9 and 10). We first focus on the 2004 data, for which the local acceleration, Coriolis, and curvature terms in Eq. (9) were calculated. At both sites and for all conditions, the dominant terms among these three were Coriolis and curvature forcing. However, the local acceleration term at SD was sometimes of similar magnitude, especially during flood tides. This term displayed a vertically banded pattern as cross-channel currents at different depths reached peak values and then decelerated. The patterns and sign of the combination of curvature and Coriolis forcing were consistent with driving the observed patterns in the cross-channel flows, including the multilayer flows at the ebb to flood transition, the two- or three-layer flows during flood tides and the two-layer flows during spring ebbs at LH.

The residual was large at times, of the same magnitude as the dominant measured forcing terms. This indicates that some combination of the unmeasured momentum terms (vertical stress divergence, baroclinic pressure gradient, and advection) must be significant. These terms must have balanced Coriolis and curvature when their combined forcing exceeded the observed local acceleration. Due to stronger along-channel currents, spring tides had larger Coriolis and curvature forcing than neap tides, as well as larger residuals overall. Low- and high-discharge balances were similar, with slightly larger residuals at LH during high-discharge spring tides.

The two sites showed a different relationship between Coriolis and curvature forcing. At SD (upper panels in Figs. 9 and 10), the two terms were additive during flood tide, resulting in a large residual where their combined forcing surpassed the observed local acceleration. However, during ebb, Coriolis and

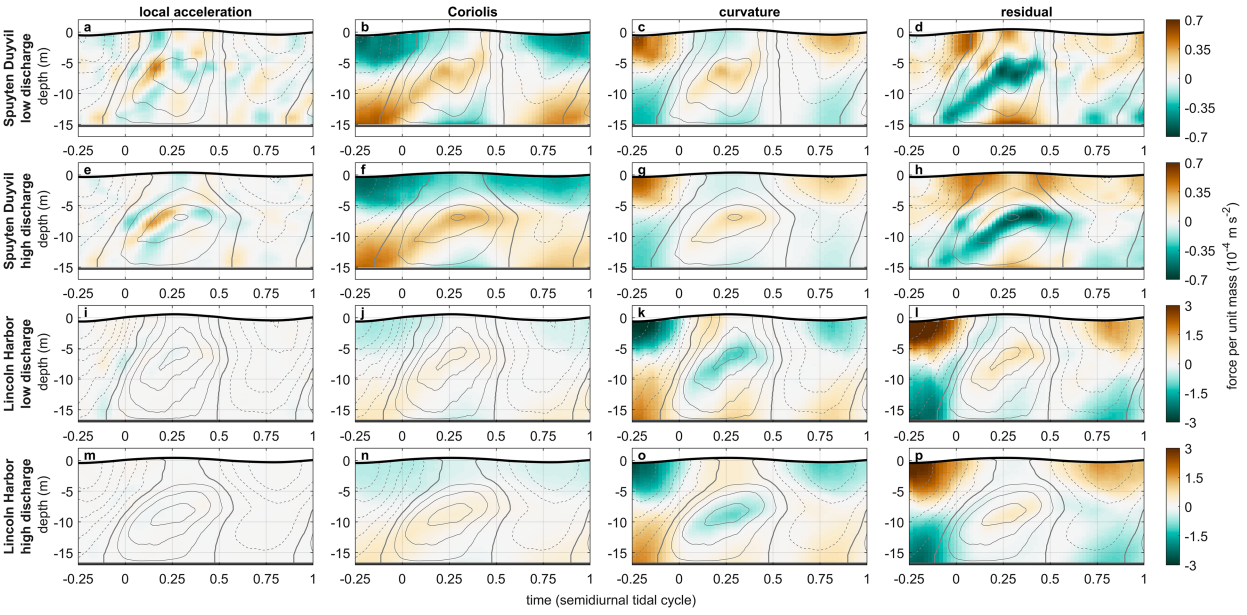

FIG. 10. Semidiurnal phase-averaged cross-channel momentum balance terms (with the depth average removed) during low- and high-discharge neap tides at (a)–(h) SD and (i)–(p) LH for the 2004 study period. Axes, contouring, and shading are the same as in Fig. 9. Note that scales differ between the two sites.

curvature mostly canceled each other, resulting in a small residual. At LH (lower panels in Figs. 9 and 10), the curvature term was larger in magnitude and of opposite sign than at SD. This resulted in Coriolis and curvature only partially canceling each other during flood tides, with a large residual remaining, especially during spring tides when along-channel currents were strong and curvature forcing greatly exceeded Coriolis forcing. During ebb tide, the additive combination of Coriolis and curvature (and thus the residual) was particularly large.

The 2002 momentum balances at SD indicated that cross-channel advection can play an important role only at certain times in the tidal cycle. The terms measured in the thalweg in both years (local acceleration, Coriolis, and curvature forcing) were similar, comparing the upper 10 m of the water column where 2002 terms were calculated, but contributions from cross-channel advection slightly altered the structure of the residual (Fig. 11). Cross-channel advection was generally small compared to Coriolis and curvature, but took on greater importance during peak flood tide in the thalweg region (Figs. 11d,i), slightly reducing the residual relative to 2004. The balance on the shoal was similar to the thalweg balance during spring tides, except compressed into a smaller water depth, whereas during neap tides the advective forcing was weaker (Fig. 12). As in 2004, the residual was large at times, especially during flood tides, indicating a leading-order importance for some combination of vertical stress divergence, along-channel and vertical advection, and the baroclinic pressure gradient (see section 4c for further discussion).

Cross-channel density gradients calculated for the 2002 data showed differences in horizontal density structure between

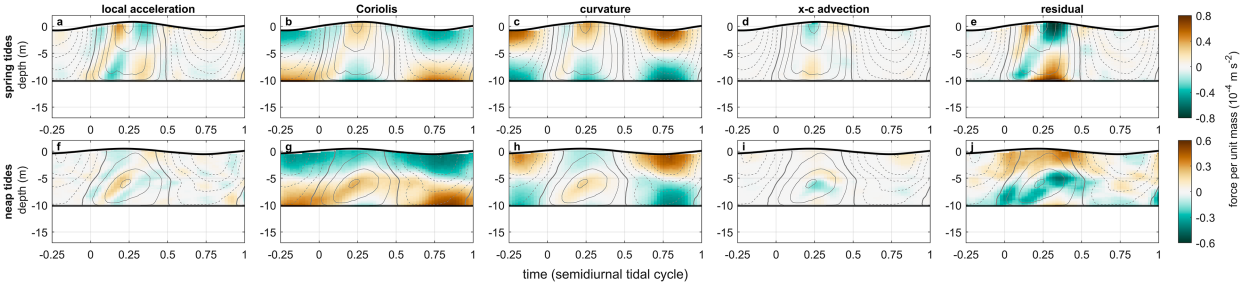

FIG. 11. Semidiurnal phase-averaged cross-channel momentum balance terms (with the depth average removed) for the thalweg region at SD in 2002. Time runs from just before the beginning of flood to the end of ebb. Depth ranges from zero at the mean water surface to the depth at site 3. Values are only shown for depths where data were available on both sides of the region. The magnitude of each term is shown in color, with brown (green) indicating eastward (westward) forcing. The residual is calculated as the first panel minus the subsequent three panels. Note that scales differ between the two rows. Contours show the average along-channel flow (solid lines for flooding flow and dashed lines for ebbing flow at 0.25 m s^{-1} intervals, with a thicker solid line at zero flow).

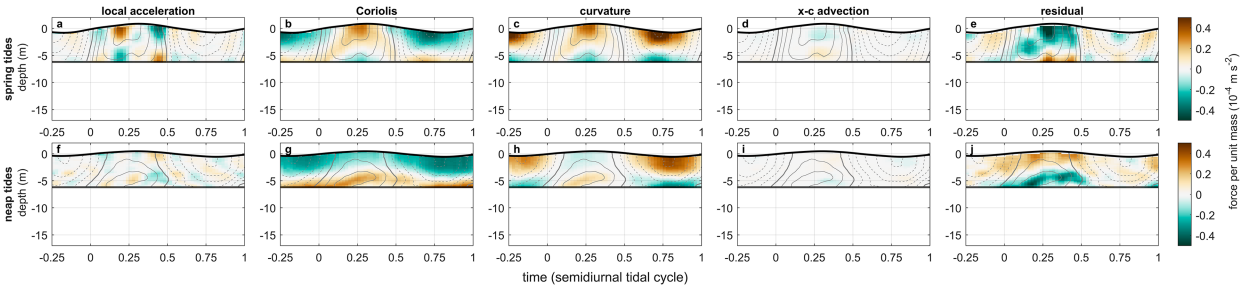

FIG. 12. Semidiurnal phase-averaged cross-channel momentum balance terms (with the depth average removed) for the shoal region at SD in 2002. Depth ranges from zero at the mean water surface to the depth at site 1. Axes, shading, and contouring are the same as in Fig. 11.

spring and neap tides as well as between shoal and thalweg regions, providing some qualitative insight into baroclinic forcing [see section 2e(1) for more details]. Cross-channel density gradients across both regions were minimal during spring tides, with a tendency for density to increase moving eastward (Figs. 13a,b). These positive gradients, especially during ebb tides in the thalweg, would tend to produce near-surface eastward acceleration (Figs. 13e,f). Strong vertical stratification during neap tides coincided with strong horizontal gradients, especially across the thalweg region (Figs. 13c,d). During flood tide, denser water was present on both the western and eastern banks around 5 m depth relative to the center of the channel, indicated by the opposing signs of $\Delta\rho/\Delta x$ in the shoal and thalweg regions (Figs. 13c,d, times 0–0.5). This would generate opposite tendencies in the two regions, with an eastward over westward pattern in the thalweg (Fig. 13g). Dense water moved up onto the shoal during ebb tide, producing a middepth maximum in density near the middle of the channel (Figs. 13c,d, times 0.5–1), while surface

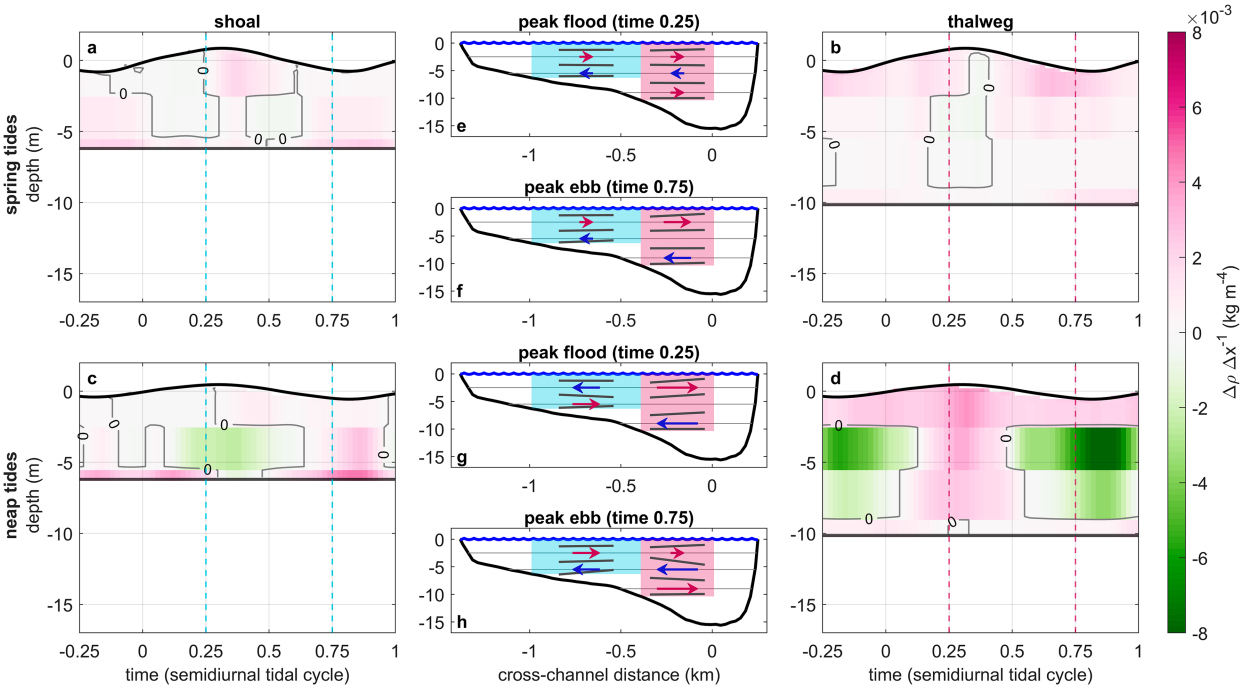

FIG. 13. Semidiurnal phase-averaged cross-channel density gradients across the (a),(c) shoal and (b),(d) thalweg regions at SD for the 2002 study period. (top) Spring tides and (bottom) neap tides are shown. Thick black lines indicate the water surface height and the bottom depth for each region as defined in Fig. 2a, which corresponds to the maximum depth where data is available on both sides of each region. Time starts just before the transition from ebb to flood and ends at the end of ebb. Vertical dashed lines show the times depicted in the schematic diagrams. (e)–(h) Schematics show isopycnal tilting (thick gray line segments) and inferred cross-channel tendencies (red and blue arrows) based on the sign and magnitude of cross-channel density gradients. Each panel represents a cross-sectional view of the channel at SD, with a wavy blue line at the water surface and a thick black line at the estuary bed. Thin gray lines show the vertical boundaries of the regions where density was calculated. The shoal and thalweg regions are shaded in turquoise and red, respectively. Panels (e) and (f) show peak flood (time 0.25) and peak ebb (time 0.75) during spring tides, and (g) and (h) show the same for neap tides. Blue (red) arrows indicate westward (eastward) tendencies.

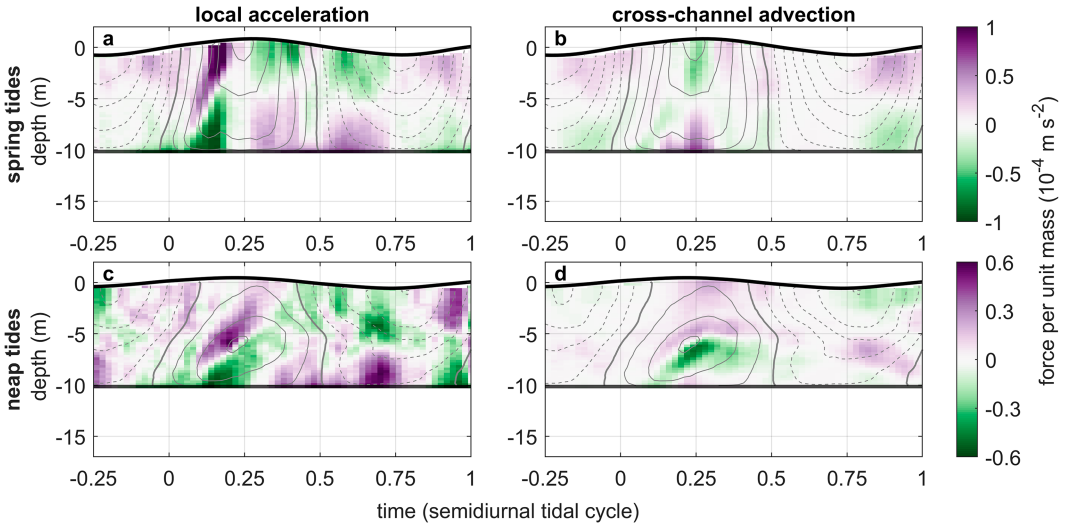

FIG. 14. Semidiurnal phase-averaged along-channel momentum balance terms (with the depth average removed) for the thalweg region at SD in 2002. Time runs from just before the start of flood to the end of ebb. Depth ranges from zero at the mean water surface to the depth at site 3. Values are only shown for depths where data were available on both sides of the region. The magnitude of each term is shown in color, with purple (green) indicating landward (oceanward) forcing. Note that scales differ between the two rows. Contours show the average along-channel flow (solid lines for flooding flow and dashed lines for ebbing flow at 0.25 m s^{-1} intervals, with a thicker solid line at zero flow).

water remained denser to the east throughout the tidal cycle. These density gradients would produce strong westward tendencies at middepths during peak ebb, with corresponding eastward tendencies near the bottom and the surface (Fig. 13h).

2) ALONG-CHANNEL MOMENTUM BALANCE

In the along-channel momentum balance for the SD 2002 data (with the depth average removed), local acceleration and cross-channel advection had similar magnitudes (Figs. 14 and 15). Cross-channel advection of the along-channel flow in the thalweg region was especially important at middepths during flooding neap tides (Fig. 14d), as well as throughout the water column during peak flood and the later half of ebb for spring tides (Fig. 14b). In the shoal region, cross-channel advection was generally weak except for flooding spring tides, when advection worked against landward flow near the surface while accelerating it near the bottom (Fig. 15b). This feature dominated the tidally averaged cross-channel advection, producing a net oceanward

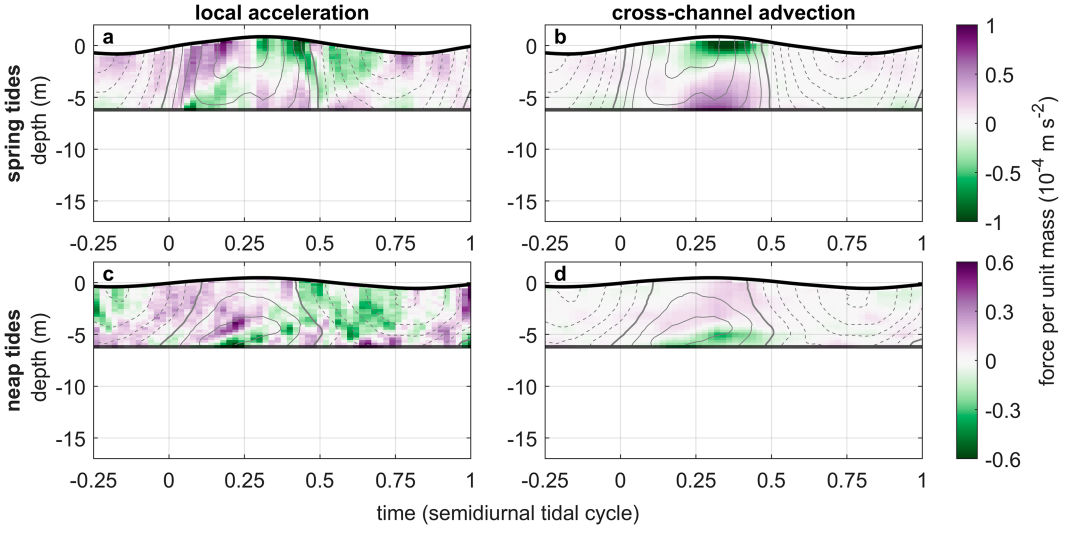

FIG. 15. Semidiurnal phase-averaged along-channel momentum balance terms (with the depth average removed) for the shoal region at SD in 2002. Depth ranges from zero at the mean water surface to the depth at site 1. Axes, contouring, and shading are the same as in Fig. 14. Note that scales differ between the two rows.

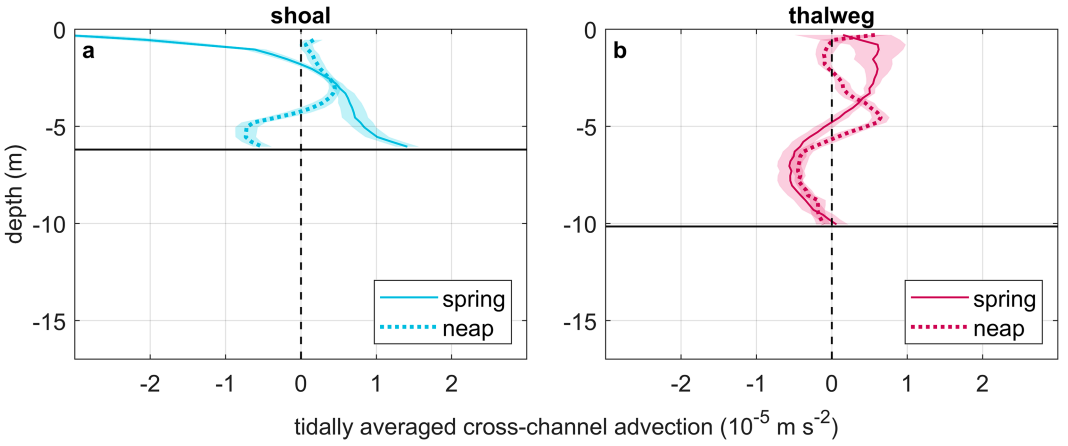

FIG. 16. Tidally averaged cross-channel advection of cross-channel gradients in the along-channel flow [$u(\partial v/\partial x)$ with the depth average removed] for the (left) shoal and (right) thalweg regions at SD in 2002. Depth ranges from zero at the mean water surface to the depth at site 1 (left) and at site 3 (right). Positive (negative) values indicate landward (oceanward) forcing. Solid (dotted) lines show spring (neap) tide values. Shading around each line shows ±1 standard deviation of the mean value at each depth based on a bootstrapping estimate using 10 000 random samples with replacement from the set of 8 (neap) or 10 (spring) available tidal cycles.

acceleration at the surface and landward acceleration near the bottom for the shoal region during spring tides, in contrast to the opposite pattern for the thalweg region during spring tides and weaker, more complex patterns for neap tides (Fig. 16).

4. Discussion

a. *Influence of tidal amplitude, river discharge, and stratification on along- and cross-channel flows*

Along-channel flows showed distinct patterns linked to stratification changes driven by tidal amplitude and river discharge. During periods of low stratification, including most spring tides and especially those with low discharge, peak flood and ebb along-channel flows were fastest at the surface. However, when stratification was strong, during neap tides and some spring tides with high discharge, the maximum in along-channel flow shifted to a middepth location during flood, returning to the surface during ebb tide (Fig. 7). This pattern is consistent with Geyer et al. (2000) and Chant et al. (2007), who also observed subsurface maxima in peak flood currents during neap tides in the Hudson. They found that strong stratification restricts the influence of bottom stress to depths below the pycnocline, leading to low stress near the surface. In contrast to neap floods, observations using dye indicated weak mixing throughout the water column during neap ebbs and spring tide boundary layers that extended to the surface (Chant et al. 2007).

The patterns of cross-channel flow at both sites also demonstrated the strong influence of stratification. During all conditions, Coriolis and curvature dominated the measured momentum balance terms. Their combination was generally consistent with driving the observed currents, including a switch from two-layer flows during more mixed conditions to three-layer flows during more stratified conditions (Fig. 7). Two- and three-layer patterns of flow were also observed by Chant (2002) and Nidzieko et al. (2009), but the forces driving flow patterns in those studies may not explain the dynamics observed here. Both studies' sites had stronger curvature than LH and SD, with values of $|\gamma|$ that we estimate to be larger than 10 compared to $|\gamma| < 4$ for all conditions observed at our sites (Table 1). In Nidzieko et al. (2009), three-layer flows developed as a two-layer curvature-forced flow tilted isopycnals, generating baroclinic pressure gradients that altered the initial flow pattern. Chant (2002) hypothesized a similar mechanism. However, we observed well-developed three-layer flows that remained fairly consistent throughout flood tide, suggesting that any baroclinic forcing was not large enough to reverse curvature and Coriolis forcing. Instead, the local vertical structure of the along-channel flow produced combined Coriolis and curvature forcing patterns that supplied the necessary acceleration to produce the observed two- and three-layer flows.

Contrasts in flow between flood and ebb tides further support the key role of stratification in cross-channel flow structure. Curvature and Coriolis forcing share the same sign during ebb tides at LH, generally leading to stronger ebb cross-channel flows. However, this was only true during spring tides, when stratification was weak (Figs. 7e,f). During neap tides, cross-channel flows were stronger during flood than ebb (Figs. 7g,h), despite stronger curvature plus Coriolis forcing during ebb (Figs. 10l,p). Strong stratification and lateral tilting of the pycnocline could produce baroclinic pressure gradients that suppress ebb tide cross-channel flows (Lerczak and Geyer 2004). However, stratification did not prevent the

TABLE 1. Values of γ for the two sites under different tidal amplitude (spring or neap) and discharge (low or high) conditions.

	Spring low	Spring high	Neap low	Neap high
SD	0.86	0.90	0.49	0.37
LH	−3.66	−3.60	−1.87	−1.46

formation of a clear three-layer flow during neap flood tides, even as Coriolis forcing counteracted curvature forcing. This three-layer flow pattern would not tilt the pycnocline as a two-layer pattern would, because flow in the middle layer that reaches the western bank must move both upward and downward. Therefore, baroclinic pressure gradients may be unable to suppress the three-layer flow characteristic of flood tides, unlike the two-layer flow during ebb tides.

b. *Site differences in along- and cross-channel flows*

Along-channel flows were similar in pattern and magnitude at the two sites with one distinguishing characteristic. A subsurface maximum in along-channel flow occurred during spring flood tides with high discharge at LH (Fig. 7f), resembling neap flood tides, whereas SD had similar along-channel flow during spring tides regardless of discharge (Figs. 7a,b). We observed higher stratification at LH than at SD during high-discharge conditions (Figs. 5b,f,d,h), perhaps because LH is located closer to the estuary mouth. This likely drives the observed three-layer cross-channel flow pattern during LH high-discharge spring flood tides, resembling the three-layer patterns characteristic of more stratified neap flood tides.

Differing relative magnitudes and signs of Coriolis and curvature forcing drove differences in cross-channel flow between the two sites. Values of γ under different regimes show that curvature was relatively more important at LH under all conditions, accentuated during periods of especially strong along-channel flow such as spring tides (Table 1). This drove strong cross-channel currents during both flood and ebb at LH, although Coriolis slightly counteracted curvature forcing during flood, leading to stronger ebb flows during spring tides. Stratification altered this dynamic during neap tides, as previously discussed. At SD, curvature was slightly less important than Coriolis, but neared equal strength during spring tides due to the quadratic dependence of curvature on along-channel flow. Coriolis and curvature tended to cancel each other during ebb, leading to stronger flood tide flows. However, some weak two-layer flows developed during spring tide ebbs (Fig. 8d, times 0.65–0.9) in a direction consistent with being driven by curvature. They may reflect curvature forcing briefly outweighing Coriolis forcing during peak ebb flows, or they may be related to baroclinic forcing; density gradients suggest denser water to the east during spring ebbs, producing an eastward acceleration at the surface (Figs. 13b,f).

Determining the radius of curvature adds uncertainty to the momentum balance. It is difficult to define what radius the majority of the flow experiences as it rounds each bend, especially for larger-radius curves as observed in this study. The appropriate radius may also differ between flood and ebb because of differences in shape between the upstream and downstream sides of the curve. A larger radius at LH would slightly reduce the residuals, but the patterns of flow, with strong flood currents despite Coriolis counteracting curvature, suggest that curvature should indeed outweigh Coriolis at this site. Overall, the radii used in our calculations are consistent with the observed patterns of flow.

c. *Closing the cross-channel momentum balance*

The combination of Coriolis and curvature forcing produced patterns that were consistent with accelerating the observed cross-channel flow patterns in the correct directions. However, during certain tidal stages and forcing regimes, a large residual in the cross-channel momentum balance persisted. This indicates the importance of some combination of vertical stress divergence, baroclinic pressure gradients, and advection in balancing Coriolis and curvature forcing. As the cross-channel flow accelerated to peak values, these unmeasured terms likely increased in importance, counteracting further local acceleration driven by Coriolis and curvature and resulting in the fairly steady cross-channel momentum balance (small local accelerations) observed during peak flood and ebb.

The 2002 SD momentum balance shows that cross-channel advection was not sufficient to balance the observed accelerations driven by Coriolis and curvature. Cross-channel advection did not play a major role except close to areas of strong acceleration, such as peak flood currents (Figs. 11d,i, for example). Similar to our observations, modeling supports an increase in the importance of cross-channel advection during less stratified conditions and near maximum flood, but a more dominant role for vertical stress divergence and pressure gradients throughout the tidal cycle and especially during stratified conditions (Lerczak and Geyer 2004).

Along-channel and vertical advection may be significant terms in the cross-channel momentum balance. Because of the gradually curving channel and the large distance between curves, along-channel advection is unlikely to be as strong as observed by Nidzieko et al. (2009) and Kranenburg et al. (2019) in sharper bends, but could nevertheless be significant at certain times. Along-channel advection is likely more important at LH than at SD due to stronger curvature forcing causing more rapid change in u moving through the bend, compared to the background cross-channel flow driven by Coriolis that must be present throughout the channel, varying slightly with along-channel flow structure. A rough estimate of along-channel advection, making the assumption that the cross-channel flow at each site develops from zero flow at the entrance of each bend over the distance Δy to the measurement site (therefore ignoring the influence of Coriolis), can be calculated as $V(\Delta U/\Delta y)$. For example, at LH, using maximum flows of $\Delta U = 0.3$ m s^{-1} and $V = 2$ m s^{-1} yields a momentum balance term of the same order as Coriolis and curvature during peak flows. A more conservative estimate assuming a linear gradient in cross-channel flow between LH and SD is an order of magnitude smaller. Greater along-channel resolution is necessary to determine the importance of this term. Vertical advection could also be important during peak flows when distinct layers result in strong vertical gradients in u, and when vertical motion is necessary to close cross-channel circulation cells. For example, a vertical flow of 0.01 m s^{-1}, combined with the vertical gradients during peak ebb or flood, would produce a leading-order momentum balance term.

The tilting of isopycnals by the cross-channel flow could generate strong baroclinic gradients that help balance Coriolis

and curvature forcing, especially during more stratified neap tides. Past studies have found baroclinic forcing to be of leading-order importance in the cross-channel momentum balance (Lacy and Monismith 2001; Nidzieko et al. 2009; Kranenburg et al. 2019). Although the density data resolution from the 2002 observations at SD is too low to make detailed calculations of the baroclinic pressure gradient, a rough estimate suggests that the baroclinic term is of the same order as Coriolis and curvature during neap tides, with smaller values during spring tides. During neap tides in the thalweg region, denser water to the east during flood (Fig. 13d) could reflect cross-channel flow tilting isopycnals upward in the upper 10 m through vertical flow linking middepth eastward flow with surface westward flow. The induced density forcing would counteract combined Coriolis and curvature forcing, perhaps helping to balance the budget (Figs. 13g and 11j). Denser water appeared to accumulate at middepth near the middle of the channel during neap ebbs (Figs. 13c,d, times 0.5–1), perhaps advected by westward flow near the bottom during flood tide, but the resulting tendency for middepth westward flow and near-bottom eastward flow is not reflected in the cross-channel flow patterns (Figs. 13h and 8e–h). Due to the low resolution of our density data, the vertical extent of large horizontal gradients in density may be spread over a larger depth range than is accurate. Overall, higher-resolution density measurements are needed to fully address the role of baroclinic gradients.

Finally, vertical stress divergence likely plays a key role in balancing the cross-channel momentum budget. This term could balance driving forces, especially lower in the water column and during more mixed periods when the eddy viscosity is enhanced (Geyer et al. 2000). Modeling by Lerczak and Geyer (2004) and Scully et al. (2009) supports a strong influence from stress divergence, in particular during flood tides and near the bottom. Using eddy viscosity profiles calculated by Geyer et al. (2000) with rough estimates for the vertical gradient in cross-channel flow yields a leading-order momentum balance term during spring flooding tides, when the residual tends to be large (Fig. 9). We were unable to calculate the second derivative of u from our data due to excessive noise, precluding a more accurate estimate of the importance of this term.

d. *Implications for broader estuarine dynamics*

Based on the magnitude of cross-channel currents over a tidal cycle, cross-channel flows had a stronger influence on broader estuarine dynamics at LH than at SD. Values of β reveal that this influence was greater during spring tides than neap tides (Table 2). However, strong cross-channel flows during the flood stage of all regimes at both sites could accomplish substantial transport. During spring tides with high discharge at LH, the cross-channel flows were especially significant, with the potential to transport material completely across the channel within a few hours.

During spring tides at LH, β was larger during high discharge than low discharge, despite stratification being slightly higher (Figs. 5e,f). During these weakly stratified conditions, a small increase in stratification could enhance cross-channel flows by reducing mixing and decreasing the eddy viscosity, as in Buijsman and Ridderinkhof (2008) and Geyer (1993). For the same curvature plus Coriolis forcing, a decrease in eddy viscosity caused by increasing stratification allows for an increase in the vertical shear and therefore the magnitude of the cross-channel flows to maintain the same stress divergence. This mechanism could explain the stronger high-discharge cross-channel flows for LH spring tides.

TABLE 2. Values of β for the two sites under different tidal amplitude (spring or neap) and discharge (low or high) conditions.

	Spring low	Spring high	Neap low	Neap high
SD	0.33	0.32	0.26	0.19
LH	0.77	0.99	0.40	0.34

Flood–ebb asymmetry in cross-channel flows could affect sediment transport. Fugate et al. (2007) observed stronger cross-channel flows during one stage of the tide in upper Chesapeake Bay, which combined with stratification dynamics to concentrate sediment on one side of the channel. At SD, strong westward cross-channel flows near the bed during spring flood tides (Figs. 7a,b), paired with stronger spring tide along-channel flows that resuspend sediment, could preferentially move bottom sediment toward the west bank, perhaps contributing to the development of the shallow western shoal (Geyer et al. 1998, 2001). Dredging at LH ensures a more symmetrical channel regardless of natural sediment transport.

Cross-channel advection of cross-channel gradients in the along-channel flow played an important role in the along-channel momentum balance at certain times, especially during spring tides when the currents were strongest. During flood tide, the cross-channel flow advected low-momentum water from the western bank eastward across the channel at the surface while moving high-momentum water from the thalweg westward onto the shoal at depth. This enhanced the exchange flow on the shoal by slowing landward flows near the surface and accelerating landward flows at depth (Fig. 15b). In the thalweg, a similar effect occurred near peak flood, but the opposite occurred during late ebb, when oceanward flows at the surface were slowed by advection of slow water from the shoal (Fig. 14b). This produced an overall weakening of the exchange flow (excluding unknown effects in the deepest 5 m of the channel) as evidenced by the tidal average, in contrast to a net strengthening on the shoal (Fig. 16). This is consistent with modeling by Lerczak and Geyer (2004), who observed peaks in cross-channel advection just after peak ebb and flood and who calculated a larger impact of tidal-averaged cross-channel advection on the exchange flow away from the thalweg. The tidally averaged cross-channel advection for spring tides on the shoal (Fig. 16a) is consistent with values modeled by Scully et al. (2009) and similar in magnitude to their modeled subtidal along-channel pressure gradient, reinforcing the importance of cross-channel advection in the along-channel balance.

5. Summary and conclusions

This study examines cross-channel flows in a curved estuarine channel with radii that fall between most examples in

published research, in which curvature is either much less important (Valle-Levinson et al. 2000; Ott et al. 2002) or much more important (Nidzieko et al. 2009; Kranenburg et al. 2019) than Coriolis forcing. Even with gradual curves, curvature forcing can assume leading-order importance in the cross-channel momentum balance, driving spatial changes in the direction and magnitude of cross-channel flows that can have important impacts on broader estuarine dynamics. Cross-channel flows also vary temporally because of variations in tidal amplitude, river discharge, and stratification. These changes in stratification impact the vertical structure of the along-channel flow, which in turn impacts the structure of the Coriolis and curvature forcing of the cross-channel flows, driving two-layer cross-channel flows when the water column is more homogeneous and three-layer flows when it is more stratified. In addition, the combination of curvature and Coriolis with similar magnitudes, combined with varying stratification, produces flood–ebb asymmetry in forcing and cross-channel flow strength that could have important impacts on transport and dispersion of water-borne materials in estuaries.

The cross-channel momentum balance reveals the dominant importance of Coriolis and curvature in generating these patterns of flow. However, large imbalances between these terms confirm that other forcing terms are essential to close the budget. Although local acceleration and cross-channel advection are of comparable magnitude to Coriolis and curvature at a few times and locations, they are not broadly important throughout the tidal cycle. Rather, some combination of vertical stress divergence, baroclinic forcing, vertical advection, and along-channel advection must balance the budget. Vertical stress divergence, enhanced by high eddy viscosity especially when stratification is low (Geyer et al. 2000), is a likely contributor, as well as the tilting of isopycnals by the vertical motion required to complete cross-channel circulation cells. Vertical advection by this same motion and along-channel advection of gradients in the cross-channel flow could also play a role. More detailed observations are necessary to fully characterize these dynamics.

Acknowledgments. Data collection was supported by NSF Grant OCE-0095972 and Hudson River Foundation Grant 005/03A. Data analysis and manuscript preparation were supported by NSF Grants OCE-1829979, OCE-1949067, and OCE-2219928 and by the U.S. Department of Energy, Office of Science, Biological and Environmental Research through the collaborative, multiprogram Integrated Coastal Modeling (ICoM) project. We thank the reviewers, Nick Nidzieko and Wouter Kranenburg, for thoughtful comments that strengthened the manuscript.

Data availability statement. Data analyzed in this study are openly available from the WHOAS (Woods Hole Open Access Server) at https://hdl.handle.net/1912/66651 (2004 data, DOI 10.26025/1912/66651) and https://hdl.handle.net/1912/66838 (2002 data, DOI 10.26025/1912/66838). Data on Hudson River discharge are available from the USGS Water Data for the Nation at https://doi.org/10.5066/F7P55KJN (site identification number 01358000).

REFERENCES

Alaee, M. J., G. Ivey, and C. Pattiaratchi, 2004: Secondary circulation induced by flow curvature and Coriolis effects around headlands and islands. *Ocean Dyn.*, **54**, 27–38, https://doi.org/10.1007/s10236-003-0058-3.

Bathurst, J. C., C. R. Thorne, and R. D. Hey, 1977: Direct measurements of secondary currents in river bends. *Nature*, **269**, 504–506, https://doi.org/10.1038/269504a0.

Buijsman, M. C., and H. Ridderinkhof, 2008: Variability of secondary currents in a weakly stratified tidal inlet with low curvature. *Cont. Shelf Res.*, **28**, 1711–1723, https://doi.org/10.1016/j.csr.2008.04.001.

Chant, R. J., 2002: Secondary circulation in a region of flow curvature: Relationship with tidal forcing and river discharge. *J. Geophys. Res.*, **107**, 3131, https://doi.org/10.1029/2001JC001082.

——, 2010: Estuarine secondary circulation. *Contemporary Issues in Estuarine Physics*, A. Valle-Levinson, Ed., Cambridge University Press, 100–124.

——, and R. E. Wilson, 1997: Secondary circulation in a highly stratified estuary. *J. Geophys. Res.*, **102**, 23 207–23 215, https://doi.org/10.1029/97JC00685.

——, W. R. Geyer, R. Houghton, E. Hunter, and J. Lerczak, 2007: Estuarine boundary layer mixing processes: Insights from dye experiments. *J. Phys. Oceanogr.*, **37**, 1859–1877, https://doi.org/10.1175/JPO3088.1.

Cossu, R., and M. G. Wells, 2010: Coriolis forces influence the secondary circulation of gravity currents flowing in large-scale sinuous submarine channel systems. *Geophys. Res. Lett.*, **37**, L17603, https://doi.org/10.1029/2010GL044296.

Costanza, R., and Coauthors, 1997: The value of the world's ecosystem services and natural capital. *Nature*, **387**, 253–260, https://doi.org/10.1038/387253a0.

Fugate, D. C., C. T. Friedrichs, and L. P. Sanford, 2007: Lateral dynamics and associated transport of sediment in the upper reaches of a partially mixed estuary, Chesapeake Bay, USA. *Cont. Shelf Res.*, **27**, 679–698, https://doi.org/10.1016/j.csr.2006.11.012.

Geyer, W. R., 1993: Three-dimensional tidal flow around headlands. *J. Geophys. Res.*, **98**, 955–966, https://doi.org/10.1029/92JC02270.

——, and R. Chant, 2006: The physical oceanography processes in the Hudson River estuary. *The Hudson River Estuary*, J. S. Levinton and J. R. Waldman, Eds., Cambridge University Press, 24–38.

——, and P. MacCready, 2014: The estuarine circulation. *Annu. Rev. Fluid Mech.*, **46**, 175–197, https://doi.org/10.1146/annurev-fluid-010313-141302.

——, R. P. Signell, and G. C. Kineke, 1998: Lateral trapping of sediment in a partially mixed estuary. *Physics of Estuaries and Coastal Seas: Proceedings of the 8th International Biennial Conference on Physics of Estuaries and Coastal Seas*, A. A. Balkema, 115–124.

——, J. H. Trowbridge, and M. M. Bowen, 2000: The dynamics of a partially mixed estuary. *J. Phys. Oceanogr.*, **30**, 2035–2048, https://doi.org/10.1175/1520-0485(2000)030<2035:TDOAPM>2.0.CO;2.

——, J. D. Woodruff, and P. Traykovski, 2001: Sediment transport and trapping in the Hudson River estuary. *Estuaries*, **24**, 670–679, https://doi.org/10.2307/1352875.

——, R. J. Chant, R. Houghton, J. A. Lerczak, E. J. Hunter, and M. M. Conley, 2023: Hudson River estuary 2002 field

experiment: Moorings. Woods Hole Open Access Server, accessed 20 September 2023, https://hdl.handle.net/1912/66838.

Kalkwijk, J. P. T., and R. Booij, 1986: Adaptation of secondary flow in nearly-horizontal flow. *J. Hydraul. Res.*, **24**, 19–37, https://doi.org/10.1080/00221688609499330.

Kranenburg, W. M., W. R. Geyer, A. M. P. Garcia, and D. K. Ralston, 2019: Reversed lateral circulation in a sharp estuarine bend with weak stratification. *J. Phys. Oceanogr.*, **49**, 1619–1637, https://doi.org/10.1175/JPO-D-18-0175.1.

Lacy, J. R., and S. G. Monismith, 2001: Secondary currents in a curved, stratified, estuarine channel. *J. Geophys. Res.*, **106**, 31 283–31 302, https://doi.org/10.1029/2000JC000606.

Lerczak, J. A., and W. R. Geyer, 2004: Modeling the lateral circulation in straight, stratified estuaries. *J. Phys. Oceanogr.*, **34**, 1410–1428, https://doi.org/10.1175/1520-0485(2004)034<1410:MTLCIS>2.0.CO;2.

——, ——, and R. J. Chant, 2006: Mechanisms driving the time-dependent salt flux in a partially stratified estuary. *J. Phys. Oceanogr.*, **36**, 2296–2311, https://doi.org/10.1175/JPO2959.1.

——, ——, and D. K. Ralston, 2009: The temporal response of the length of a partially stratified estuary to changes in river flow and tidal amplitude. *J. Phys. Oceanogr.*, **39**, 915–933, https://doi.org/10.1175/2008JPO3933.1.

——, D. K. Ralston, W. R. Geyer, and M. M. Conley, 2023: Hudson River estuary 2004 field experiment. Woods Hole Open Access Server, accessed 15 August 2023, https://hdl.handle.net/1912/66651.

McDougall, T. J., and P. M. Barker, 2011: Getting started with TEOS-10 and the Gibbs Seawater (GSW) Oceanographic Toolbox. Tech. Rep. SCOR/IAPSO WG127, 34 pp., https://www.teos-10.org/pubs/Getting_Started.pdf.

Nidzieko, N. J., J. L. Hench, and S. G. Monismith, 2009: Lateral circulation in well-mixed and stratified estuarine flows with curvature. *J. Phys. Oceanogr.*, **39**, 831–851, https://doi.org/10.1175/2008JPO4017.1.

Nunes, R. A., and J. H. Simpson, 1985: Axial convergence in a well-mixed estuary. *Estuarine Coastal Shelf Sci.*, **20**, 637–649, https://doi.org/10.1016/0272-7714(85)90112-X.

Ott, M. W., R. Dewey, and C. Garrett, 2002: Reynolds stresses and secondary circulation in a stratified rotating shear flow. *J. Phys. Oceanogr.*, **32**, 3249–3268, https://doi.org/10.1175/1520-0485(2002)032<3249:RSASCI>2.0.CO;2.

Pawlowicz, R., B. Beardsley, and S. Lentz, 2002: Classical tidal harmonic analysis including error estimates in MATLAB using T_tide. *Comput. Geosci.*, **28**, 929–937, https://doi.org/10.1016/S0098-3004(02)00013-4.

Ralston, D. K., W. R. Geyer, and J. A. Lerczak, 2008: Subtidal salinity and velocity in the Hudson River estuary: Observations and modeling. *J. Phys. Oceanogr.*, **38**, 753–770, https://doi.org/10.1175/2007JPO3808.1.

Rozovskii, I. L., 1957: *Flow of Water in Bends of Open Channels.* Academy of Sciences of the Ukrainian SSR, 233 pp.

Scully, M. E., W. R. Geyer, and J. A. Lerczak, 2009: The influence of lateral advection on the residual estuarine circulation: A numerical modeling study of the Hudson River estuary. *J. Phys. Oceanogr.*, **39**, 107–124, https://doi.org/10.1175/2008JPO3952.1.

Seim, H. E., and M. C. Gregg, 1997: The importance of aspiration and channel curvature in producing strong vertical mixing over a sill. *J. Geophys. Res.*, **102**, 3451–3472, https://doi.org/10.1029/96JC03415.

Simpson, J. H., J. Brown, J. Matthews, and G. Allen, 1990: Tidal straining, density currents, and stirring in the control of estuarine stratification. *Estuaries*, **13**, 125–132, https://doi.org/10.2307/1351581.

Smith, J. D., and S. R. McLean, 1984: A model for flow in meandering streams. *Water Resour. Res.*, **20**, 1301–1315, https://doi.org/10.1029/WR020i009p01301.

Smith, R., 1996: Combined effects of buoyancy and tides upon longitudinal dispersion. *Buoyancy Effects on Coastal and Estuarine Dynamics*, D. G. Aubrey and C. T. Friedrichs, Eds., Amer. Geophys. Union, 319–329.

U.S. Geological Survey, 2016: National Water Information System. USGS Water Data for the Nation, accessed 12 July 2004, https://waterdata.usgs.gov/monitoring-location/01358000/.

Valle-Levinson, A., K.-C. Wong, and K. M. M. Lwiza, 2000: Fortnightly variability in the transverse dynamics of a coastal plain estuary. *J. Geophys. Res.*, **105**, 3413–3424, https://doi.org/10.1029/1999JC900307.